Zero thermal expansion in YbGaGe due to an electronic valence transition

James R. Salvador[1], **Fu Guo**[2], **Tim Hogan**[2] & **Mercouri G. Kanatzidis**[1]

[1]*Department of Chemistry and Centre for Fundamental Materials Research, and*
[2]*Department of Electrical and Computer Engineering, Michigan State University, East Lansing, Michigan 48824, USA*

Most materials expand upon heating. Although rare, some materials expand on cooling, and are said to exhibit negative thermal expansion (NTE); but the property is exhibited in only one crystallographic direction. Such materials include silicon and germanium[1] at very low temperature (<100 K) and, at room temperature, glasses in the titania–silica family[2], Kevlar, carbon fibres, anisotropic Invar Fe-Ni alloys[3], ZrW_2O_3 (ref. 4) and certain molecular networks[5]. NTE materials can be combined with materials demonstrating a positive thermal expansion coefficient to fabricate composites exhibiting an overall zero thermal expansion (ZTE). ZTE materials are useful because they do not undergo thermal shock on rapid heating or cooling. The need for such composites could be avoided if ZTE materials were available in a pure form. Here we show that an electrically conductive intermetallic compound, YbGaGe, can exhibit nearly ZTE—that is, negligible volume change between 100 and 400 K. We suggest that this response is due to a temperature-induced valence transition in the Yb atoms. ZTE materials are desirable to prevent or reduce resulting strain or internal stresses in systems subject to large temperature fluctuations, such as in space applications and thermomechanical actuators.

YbGaGe and YbGaSn crystallize in the hexagonal $P6_3/mmc$ space group (MoC_2 according to Pearson's structure type)[6] (see ref. 7 and references therein). The structure is a derivative of the MgB_2 structure type and is characterized by puckered boron nitride-like GaGe and GaSn layers (for example, A, B, C and D in Fig. 1a). In YbGaGe, the Ga and Ge positions could not be distinguished from the X-ray data and the assignment was made on the basis of expected bond distances around these atoms and by analogy to the assignment of YbGaSn. The bond distances within the layers for Ga–Ge and Ga–Sn are 2.520(1)Å and 2.696(1)Å respectively, indicating strong bonding.

There are four such layers in the unit cell, ordering in an ABCD fashion. The AB and CD layers form respective pairs sandwiching the Yb(1) atoms. Within each pair—AB and CD—the Ga atoms are in alignment (that is, they face each other) so that they present the closest approach between layers in each pair and provide the binding site for the Yb(1) atoms. The Yb(2) atoms are found between the AB and CD pairs and bind to Ge or Sn atoms (Fig. 1a). Yb(1) has a trigonal prismatic coordination of Ga atoms (Fig. 1c), with bond distances of 2.921(2)Å in YbGaGe and 2.966(2)Å in YbGaSn.

This anomalously large difference between the Yb(1)–Ga bond distances in the two compounds was a first indication of the unusual nature of YbGaGe. Yb(2) is coordinated octahedrally by Ge (or Sn) atoms with distances of 3.078(1)Å and 3.238(1)Å respectively (Fig. 1d). Valence bond sum calculations, carried out to assess the oxidation state of the Yb ions in YbGaSn and YbGaGe, showed that both ions in YbGaSn were in the +2 oxidation state; in YbGaGe, however, Yb(1) was calculated to be +2.6 and Yb(2) was +2.0, suggesting an intermediate valence compound.

Another peculiar characteristic of these two structures that led us to investigate their properties further was the difference in the Ga–Ga distances between adjacent AB and CD layers that surround Yb(1). In YbGaSn this distance is 2.994(1)Å, and is considered short enough for a weak interaction. Despite the presence of the smaller Ge atom in YbGaGe, the Ga–Ga distance is much longer at 3.248(1)Å, and cannot be considered a bonding interaction. This lengthening is the consequence of electron transfer from a formally Yb^{2+} ion to a Ga–Ga bond, resulting in partial oxidation to Yb^{3+} and reductive cleavage of the Ga–Ga bond. The shortened Ga–Yb(1)
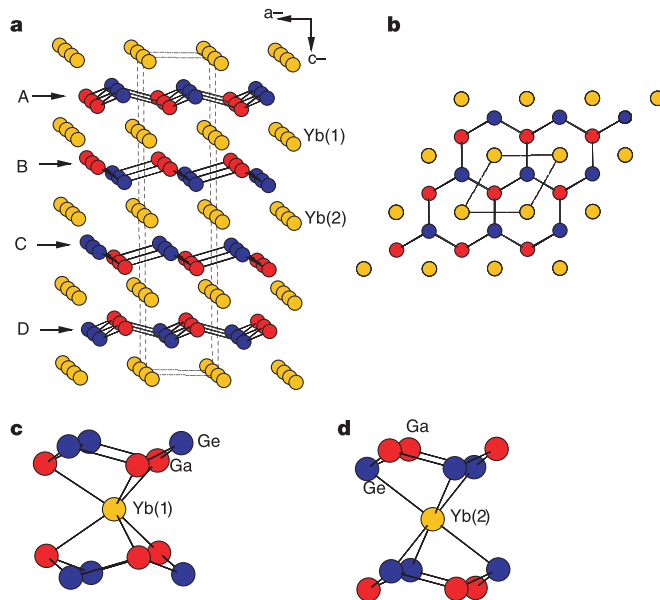

Figure 1 Crystal structure details of YbGaGe. **a**, Unit cell of YbGaGe. Red atoms are Ga, blue atoms are Ge and yellow atoms are Yb. The layers A, B, C and D are indicated. **b**, Structure viewed down the *c* axis of the $P6_3/mmc$ unit cell. **c**, Immediate trigonal prismatic coordination environment of Yb(1). **d**, Octahedral coordination of Yb(2). Atomic coordinates ($\times 10^4$) and equivalent isotropic displacement parameters ($Å^2 \times 10^3$) for

YbGaGe/YbGaSn are as follows, where U_{eq} is defined as one-third of the trace of the orthogonalized U_{ij} tensor. For Yb(1), (*x*, *y*, *z*) = (0, 0, 2,500) and U_{eq} = 14(1)/16(1). For Yb(2) (*x*, *y*, *z*) = (0, 0, 0) and U_{eq} = 10(1)/11(1). For Ge/Sn, (*x*, *y*, *z*) = (3,333, −3,333, 6,128(1)/6,146(1)) and U_{eq} = 9(1)/12(1). For Ga, (*x*, *y*, *z*) = (3,333, −3,333, 1,531(2)/1,633(2)) and U_{eq} = 14(1)/14(1).

distance and compressed c axis in the Ge analogue is due to the fact that Yb(1) in YbGaGe has mixed valency, 2+/3+, and thus has a smaller radius.

There is a certain composition width associated with the phase of YbGaGe. For example, the phase can tolerate a certain deviation from the ideal stoichiometry in the form of $YbGa_{1+x}Ge_{1-x}$ (when the material is made from Ga-rich conditions) and $YbGa_{1-x}Ge_{1+x}$ (when the material is made from Ge-rich conditions) and this is evident in
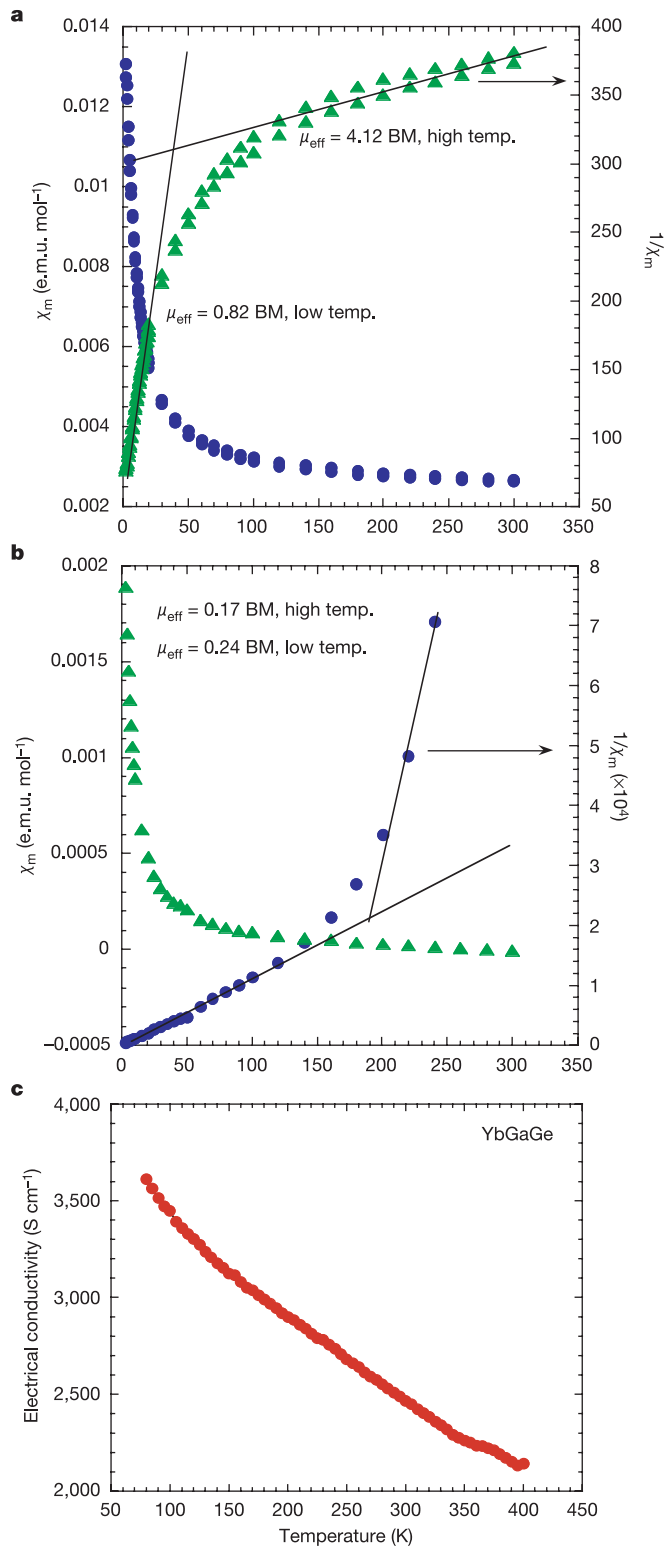
Figure 2 Magnetic susceptibility and electrical conductivity data. **a**, YbGaGe and **b**, YbGaSn (both χ_m and $1/\chi_m$). Applied field was 200 Oe for YbGaGe and 500 Oe for YbGaSn. **c**, Variable-temperature electrical conductivity for YbGaGe. Transport measurements were made using the standard four-probe configuration.
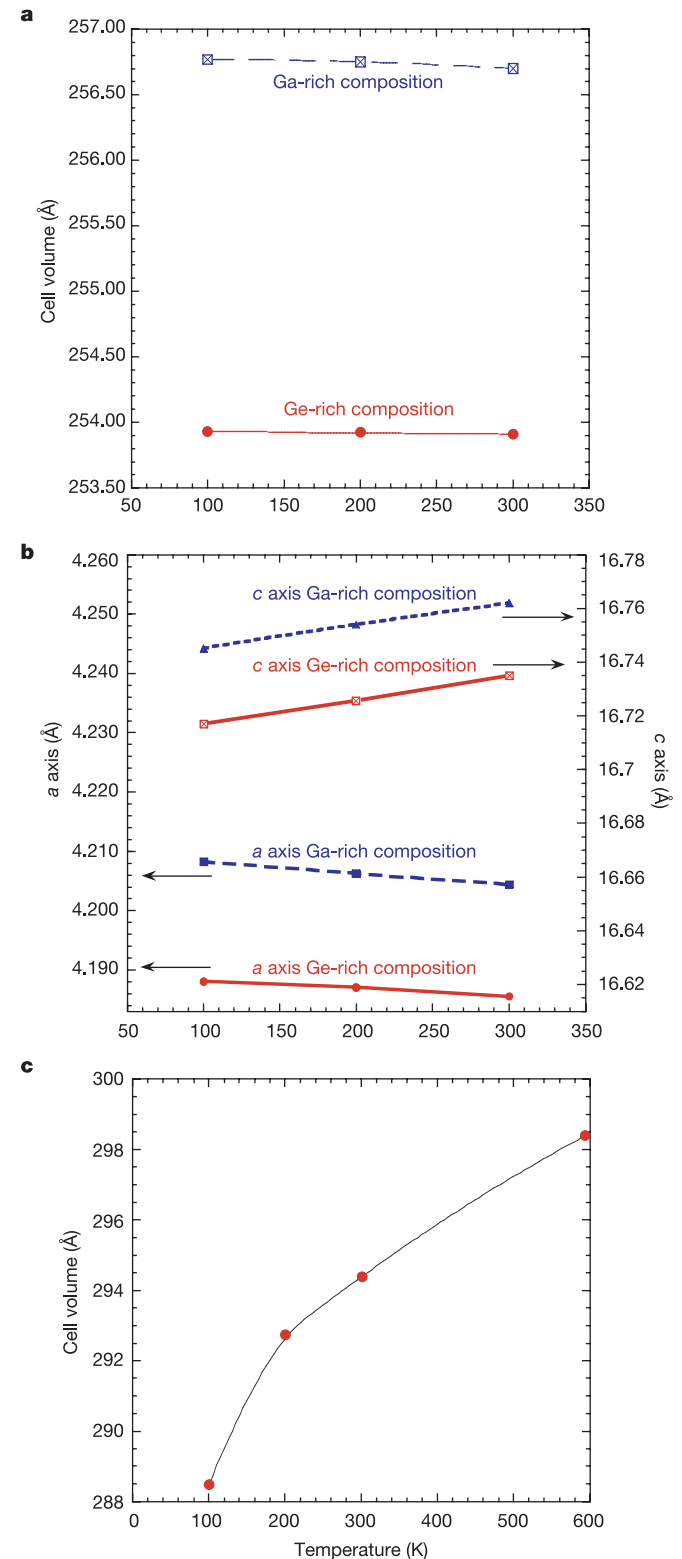
Figure 3 Thermal expansion data. **a**, Unit-cell volume versus temperature for YbGaGe. **b**, a and c cell edge lengths versus temperature for YbGaGe. **c**, Unit-cell volume versus temperature for YbGaSn. Single-crystal measurements were made by collecting a full set of data at room temperature, 200 K and 100 K. The lowest attainable temperature was 100 K. All data sets were collected on the same crystal.

the slightly different cell parameters of the crystals (for example, at 200 K, $a = 4.2064(7)$Å, $c = 16.758(5)$Å for $YbGa_{1+x}Ge_{1-x}$ versus $a = 4.1867(3)$Å, $c = 16.7275(22)$Å for $YbGa_{1-x}Ge_{1+x}$).

Crystallographic data were collected at 200 and 100 K for $YbGa_{1-x}Ge_{1+x}$ to investigate the structural changes taking place upon cooling. At 200 K, the Yb(1)–Ga bonds and the Yb(1)–Ge bonds are 2.8715(32) and 3.797(3)Å respectively and the Ga–Ge distance is 2.523(2)Å. Upon cooling to 100 K, the Yb(2)–Ge bonds both elongate to 3.0825(16)Å, while the Yb(1)–Ga is unchanged at 2.869(3)Å. The Ga–Ge distance also remains constant at 2.523(3)Å. The composition $YbGa_{1+x}Ge_{1-x}$ was measured between 200 and 300 K and it was found that the bond distances stayed constant over the temperature range, with Yb(1)–Ga distances of 2.9182(15)Å and 2.9178(15)Å at 200 and 300 K respectively, Yb(2)–Ge distances of 3.0803(16)Å and 3.0803(15)Å for 200 and 300 K respectively and Ga–Ge distances of 2.5211 Å and 2.5199(12)Å at 200 and 300 K.

Clearly, this suggests interesting behaviour in thermal expansion, which depends on the exact composition of $YbGa_{1+x}Ge_{1-x}$. We have observed overall zero volumetric thermal expansion in most samples coming from Ga-rich and Ge-rich synthetic conditions, with one showing NTE.

The critical clue for the origin of anomalous thermal expansion behaviour in YbGaGe came from the magnetic susceptibility data, which showed a temperature-induced variation in the magnetic moment of Yb atoms in this system and consequently a change in the $Yb^{2+/3+}$ ratio. The data showed an increase in the Yb^{2+} population at low temperature, indicating a volume expansion associated with the Yb^{3+} to Yb^{2+} transition. In contrast, YbGaSn is only weakly paramagnetic, with no change in the Yb^{2+} fraction (Yb^{3+} is a paramagnetic ion with calculated free ion effective magnetic moment of 4.54 BM, whereas Yb^{2+} is diamagnetic). Figure 2a shows the very different behaviour of the molar susceptibility as a function of temperature for YbGaSn and YbGaGe. YbGaGe shows a high-temperature region from 150 to 300 K that has a large μ_{eff} of $4.12\mu_B$, while below 30 K, μ_{eff} drops to only $0.82\mu_B$. The region between 30 and 150 K has a continuously changing slope and cannot be fitted to the Curie–Weiss law. This is consistent with a progressive change in Yb valence.

The magnetic data and structural data clearly show that when YbGaGe is cooled electrons move to the Yb^{3+} ions (f^{13} to f^{14} reduction) by depopulating the conduction band, thereby increasing the fraction of Yb^{2+} ions. Since Yb^{2+} is much larger than Yb^{3+} (1.16 versus 1.008 Å radius), an overall increase in the total volume is observed (see below). By comparison, YbGaSn shows a very small effective moment μ_{eff} of $0.17\mu_B$ from 100 to 300 K and $0.24\mu_B$ below 90 K (Fig. 2b). These values are consistent with predominantly Yb^{2+} in the tin analogue.

To observe the anomalous behaviour in the unit cell parameters and cell volume upon cooling, we performed X-ray diffraction experiments as a function of temperature for single crystals of $YbGa_{1+x}Ge_{1-x}$ and $YbGa_{1-x}Ge_{1+x}$. (Fig. 3a, b). Two of the unit cell constants (a, b) increase with falling temperature as expected for an expansion over the a–b plane. The c axis contracts by such an amount that the overall volume change is nearly zero (Fig. 3a). The magnitude of the NTE coefficient along the a direction was determined from the linear regression analysis of the temperature-dependent volume data to be $-1.3 \times 10^{-5} K^{-1}$ for the Ge-rich compositions and -1.8×10^{-5} for the Ga-rich compositions[3,8,9]. In contrast, YbGaSn shows a positive thermal expansion coefficient of $1.0 \times 10^{-4} K^{-1}$ (Fig. 3c).

The mechanism responsible for the NTE behaviour of ZrW_2O_8 and related oxides is geometrical in origin and has to do with cooperative rotation of the oxide tetrahedra. YbGaGe does not undergo any type of structural rotation upon cooling, as the crystal refinements at the various temperatures reveal. Instead, the NTE in YbGaGe (along the a–b plane) and the overall ZTE derive from the internal electronic charge transfer of the Yb ions in the compound.

We note that valence fluctuations were claimed as the cause for NTE coefficients, for the quasi-one-dimensional platinum compounds $[Pt(NH_3)_4][PtX_2(NH_3)_4](HSO_4)_4$ (where X = Cl, Br, I)[10].

This is a previously unknown mechanism of inducing NTE (or ZTE). One other example is $Sm_{0.9}La_{0.1}S$, which also shows an NTE coefficient of $1.4 \times 10^{-5} K^{-1}$, but only at 20 K and requires 1.7 GPa of pressure to show the effect[11]. Similarly, the compounds $CeInCu_2$ and $Ce_xLa_{1-x}Al_2$ show NTE as a result of Kondo lattice effects but it is limited to 2–10 K (refs 12, 13). The structurally identical YbGaSn has a positive thermal expansion coefficient, which lends further credence to the argument that the anomalous thermal expansion of YbGaGe is rooted in electronic causes and not in geometric configuration changes.

YbGaGe is a metallic material, with polycrystalline compactions of it showing room-temperature conductivity of $\sim$2,400 S cm^{-1}. As seen in Fig. 2c, the conductivity of YbGaGe at 77 K is approximately 3,700 S cm^{-1} and decreases to 2,200 S cm^{-1} by 400 K. By comparison, the conductivity of ZrW_2O_8 is $<10^{-8}$ S cm^{-1} at 500 K.

The very few materials that exhibit NTE (or ZTE) are insulators and can only be used as ceramics, insulators, or in optics. Thus, there is a need for new materials with similar thermal expansion behaviour over a range of temperatures but that are capable of conducting electric current. YbGaGe combines these characteristics and promises to enable new applications. Furthermore, the electronic, rather than geometric, mechanism operating in YbGaGe may possibly be exploited in the future to design other ZTE or NTE materials through the suitable selection of mixed-valency metal systems and surrounding elements. □

Methods

Synthesis of YbGaGe and YbGaSn

The pure phase of YbGaGe (which is stable in air) was obtained by directly combining the elements in their stoichiometric ratios and heating first to 850 °C for 96 h followed by quick cooling to room temperature ($\sim$23 °C) over 12 h. YbGaSn was prepared similarly by heating to 700 °C. Elemental analysis performed on several crystals indicate a Yb:Ga:Ge (or Sn) ratio of 1:1:1, consistent with the X-ray crystallographic analysis. Differential thermal analysis performed on YbGaGe showed no melting or any phase change up to 1,000 °C. Samples with excess Ga or excess Ge can be prepared accordingly by adjusting the Yb:Ga:Ge ratio.

X-ray diffraction data

Single-crystal X-ray diffraction data for YbGaGe and YbGaSn were collected at 293 K on a Siemens SMART Platform CCD diffractometer. The structure refinements were done with the SHELXTL package of crystallographic programs. Calculations were carried out with Valence Bond Calculator version 2.00 (ref. 14). $YbGa_2$ was used as the standard reference for Yb–Ga bond distances.

For YbGaGe: hexagonal $P6_3/mmc$ (no.194), $a = 4.2056(8)$Å, $c = 16.780(5)$Å, $Z = 3$, $V = 257.3(1)$Å^3, $d_{calc} = 6.112$ g cm^{-3}, $\mu = 43.28$ mm^{-1}, $2.43° < \theta(MoK_\alpha) < 26.85°$, number of total reflections = 1,352; unique reflections = 141 [$R_{int} = 0.0434$]; final R indices for all data, $R_1 = 0.0279$, w$R_2 = 7.24$ for $I > 2\sigma$.

For YbGaSn: hexagonal $P6_3/mmc$ (no.194), $a = 4.4352(9)$Å, $c = 17.291(5)$Å, $Z = 3$, $V = 294.6(1)$Å^3, $d_{calc} = 6.113$ g cm^{-3}, $\mu = 36.471$ mm^{-1}, $2.43° < \theta(MoK_\alpha) < 26.00°$, total reflections = 1,959; unique reflections = 169 [$R_{int} = 0.046$]; final R indices for all data, $R_1 = 0.036$, w$R_2 = 0.092$ for $I > 2\sigma(I)$.

1. Kagaya, H.-M. & Soma, T. Compression effect on specific heat and thermal expansion of Si and Ge. *Solid State Commun.* **85**, 617–621 (1993).
2. Schultz, P. C. & Smyth, H. T. in *Amorphous Materials* (eds Douglas, R. & Ellis, B.) (Wiley, New York, 1970).
3. Hausch, G., Bächer, R. & Hartmann, J. Influence of thermomechanical treatment on the expansion behavior of invar and superinvar. *Physica B* **161**, 22–24 (1989).
4. Mary, T. A., Evans, J. S., Vogt, O. & Sleight, A. W. Negative thermal expansion from 0.3 to 1050 Kelvin in ZrW_2O_8. *Science* **272**, 90–92 (1996).
5. Baughman, R. H. & Galvao, D. S. Crystalline network with unusual predicted mechanical and thermal properties. *Nature* **365**, 735–737 (1993).
6. Czybulka, A., Pinger, B. & Schuster, H.-U. New alkaline earth-gallium-silicides, germanides and stannides with AlB_2 type related structures. *Z. Anorg. Allg. Chem.* **579**, 151–157 (1989).
7. Hoffman, R. D. & Pöttgen, R. AlB_2-related intermetallic compounds—a comprehensive view based on group-subgroup relations. *Z. Kristallogr.* **216**, 127–145 (2001).
8. Amos, T. G. & Sleight, A. W. Negative thermal expansion in orthorhombic $NbOPO_4$. *J. Solid State Chem.* **160**, 230–232 (2001).
9. Attfield, M. P. & Sleight, A. W. Exceptional negative thermal expansion in $AlPO_4$. *Chem. Mater.* **10**, 2013–2016 (1998).
10. Tsuyoshi, M. Negative thermal expansion and valence fluctuation in quasi-one-dimensional platinum compounds. *Phys. Rev. B* **35**, 6051–6058 (1987).

11. Oomi, G., Kuwahara, R., Kagayama, T. & Jung, A. Pressure-induced volume anomaly of intermediate valence compound $Sm_{0.9}La_{0.1}S$. *J. Magn. Magn. Mater.* **226-230,** 1182–1183 (2001).

12. de Visser, A., Bakker, K. & Pierre, J. Anomalous negative thermal expansion of $CeInCu_2$. *Physica B* **186-188,** 577–579 (1993).

13. Lang, M., Schefzyk, R., Steglich, F. & Grewe, N. Negative thermal expansion in the Kondo system $Ce_xLa_{1-x}Al_2$. *J. Magn. Magn. Mater.* **63-64,** 79–81 (1987).

14. Hormillosa, C., Healy, S. & Stephen, T. *Valence Bond Calculator version 2.00* (I. D. Brown, Institute for Material Research, McMaster University, Hamilton, Ontario, Canada, 1993).

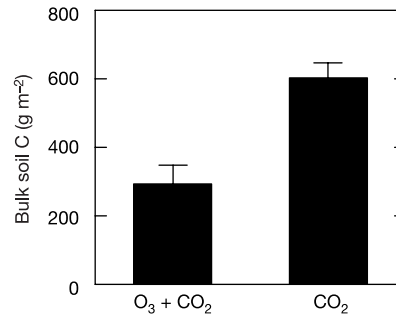**Figure 1** Total carbon incorporated into soils during 4 yr of exposure to elevated $O_3 + CO_2$ and elevated CO_2. Values are mean $\pm$ 1 s.e.; $P < 0.01$.

Reduction of soil carbon formation by tropospheric ozone under increased carbon dioxide levels

Wendy M. Loya[1], Kurt S. Pregitzer[1], Noah J. Karberg[2], John S. King[1] & Christian P. Giardina[2]

[1]*School of Forest Resources and Environmental Science, Michigan Technological University, Houghton, Michigan 49931, USA*
[2]*USDA Forest Service, North Central Research Station, Houghton, Michigan 49931, USA*

In the Northern Hemisphere, ozone levels in the troposphere have increased by 35 per cent over the past century[1], with detrimental impacts on forest[2,3] and agricultural[4] productivity, even when forest productivity has been stimulated by increased carbon dioxide levels[5]. In addition to reducing productivity, increased tropospheric ozone levels could alter terrestrial carbon cycling by lowering the quantity and quality of carbon inputs to soils. However, the influence of elevated ozone levels on soil carbon formation and decomposition are unknown. Here we examine the effects of elevated ozone levels on the formation rates of total and decay-resistant acid-insoluble soil carbon under conditions of elevated carbon dioxide levels in experimental aspen (*Populus tremuloides*) stands and mixed aspen–birch (*Betula papyrifera*) stands. With ambient concentrations of ozone and carbon dioxide both raised by 50 per cent, we find that the formation rates of total and acid-insoluble soil carbon are reduced by 50 per cent relative to the amounts entering the soil when the forests were exposed to increased carbon dioxide alone. Our results suggest that, in a world with elevated atmospheric carbon dioxide concentrations, global-scale reductions in plant productivity due to elevated ozone levels will also lower soil carbon formation rates significantly.

Large areas of the Earth are exposed to concentrations of tropospheric ozone (O_3) that exceed levels known to be toxic to plants[4,6]. In addition to reducing plant growth, exposure to elevated O_3 can also alter plant tissue chemistry[7] and reduce allocation of carbon to roots and root exudates[8–10]. Whereas the effects of O_3 on these aspects of plant biology have been widely investigated in chamber studies, examination of these effects on below-ground carbon cycling in intact forests only became possible in 1997 with the establishment of the FACTS-II (forest–atmosphere carbon transfer and storage) FACE (free-air carbon dioxide enrichment) experiment in Rhinelander, Wisconsin, USA. The long-term FACE experiment in Rhinelander examines how plant–plant and plant–microbe interactions may alter ecosystem responses to elevated O_3 and carbon dioxide (CO_2) through four treatments: control, elevated CO_2, elevated O_3 and elevated $O_3 + CO_2$. In plots where O_3 and CO_2 are elevated, concentrations were maintained at ~150% of ambient levels[11]. To examine the effects of atmospheric trace gases on both ecological interactions and on whole-ecosystem carbon cycling, each plot is split to include a pure aspen forest, a mixed aspen–birch forest and a mixed aspen–maple forest. These species were chosen because they are among the most widely distributed trees in northern temperate forests.

Here we compare soil carbon formation in aspen and aspen–birch subplots under elevated CO_2 and elevated $O_3 + CO_2$ (three plots each) to understand how exposure to O_3 under elevated CO_2 alters soil carbon formation. We used CO_2 derived from fossil fuel with its highly depleted ^{13}C signature to fumigate plant canopies in the elevated CO_2 and elevated $O_3 + CO_2$ plots. Leaf and root carbon inputs in the elevated CO_2 and elevated $O_3 + CO_2$ plots had a $\delta^{13}C$ signature of -41.6 ± 0.4‰ (mean $\pm$ s.e.) in contrast to leaf and root inputs of -27.6 ± 0.3‰ in the control plots. The $\delta^{13}C$ signature of soil carbon was -26.7 ± 0.2‰ before fumigation and

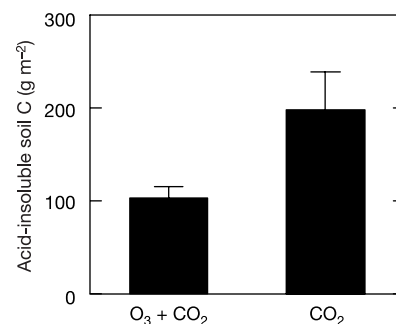**Figure 2** Carbon incorporated into the stable acid-insoluble fraction of soils during 4 yr of exposure to elevated $O_3 + CO_2$ and elevated CO_2. Values are mean $\pm$ 1 s.e.; $P < 0.01$.

Table 1 Total carbon and $\delta^{13}C$ of soils and the acid-insoluble fraction

	Total soil carbon		Acid-insoluble fraction	
	Total C (g m⁻²)	$\delta^{13}C$ (‰)	Total C (g m⁻²)	$\delta^{13}C$ (‰)
Control	5,385 ± 241	−26.7 ± 0.11	2,287 ± 185	−27.7 ± 0.06
Elevated O_3	5,237 ± 72	−26.9 ± 0.06	2,671 ± 224	−27.7 ± 0.11
Elevated CO_2	5,683 ± 480	−28.3 ± 0.10	2,594 ± 230	−29.0 ± 0.12
Elevated $O_3 + CO_2$	5,114 ± 369	−27.6 ± 0.10	2,473 ± 97	−28.5 ± 0.10

Determined for mineral soil from 0 to 20 cm. Values are mean ± s.e.